Integration and Continual Learning-Based Modeling of a Soft Robotic Sensor for Social Robot Proprioception

Pak Chuen Hau[1], Seshagopalan Thorapalli Muralidharan[1] *Student Member, IEEE*,
Randy Gomez[2] *Member, IEEE*, Georgios Andrikopoulos[1] *Member, IEEE*

***Abstract*— This paper presents an embedded soft sensor for proprioceptive feedback in a soft continuum actuator (SCA) forming the neck of the social robot HARU. The sensor is fabricated in a single-step multi-material additive manufacturing process, co-extruding conductive and non-conductive thermoplastic polyurethane to form an integrated structure. Several sensor geometries are evaluated, with a gauge-type configuration selected based on linearity and repeatability criteria. The design is embedded in a cross-configuration to measure the actuator's two dominant degrees of freedom, pitch and roll. Sensor signals are mapped to angle estimates using linear regression, a static neural network, and a continual-learning framework that updates parameters online. Experiments involving predefined trajectories, randomized motions, and repeated test cycles show that the continual-learning model achieves $R^2 > 0.97$ and mean absolute errors below 1°, consistently improving upon the baseline models. The results demonstrate the feasibility of directly embedding 3D-printed soft sensors into functional actuators and highlight the role of adaptive learning in supporting long-term soft robotic proprioception.**

I. INTRODUCTION

Soft actuators are increasingly adopted across application domains due to their inherent safety and adaptability [1]. Applications include assistive soft gloves for hand rehabilitation [2], soft robotic grippers for delicate underwater sampling [3], and soft anthropomorphic hands for complex grasping tasks [4].

A persistent challenge in soft actuation is the lack of reliable proprioceptive feedback. Accurate estimates of position and force are essential for closed-loop control but remain difficult to obtain without compromising compliance. Embedding flexible sensing elements within soft actuators has therefore become an active research direction. Among available fabrication methods, multi-material 3D printing enables integrated structures combining conductive and structural components [5]–[7]. Prior work has explored line and gauge-type printed sensors [8], [9], as well as hybrid approaches incorporating conductive filaments within external casings [10]. Despite these developments, achieving robust, multi-directional sensing suitable for actuators with multiple degrees of freedom (DoFs) remains challenging.

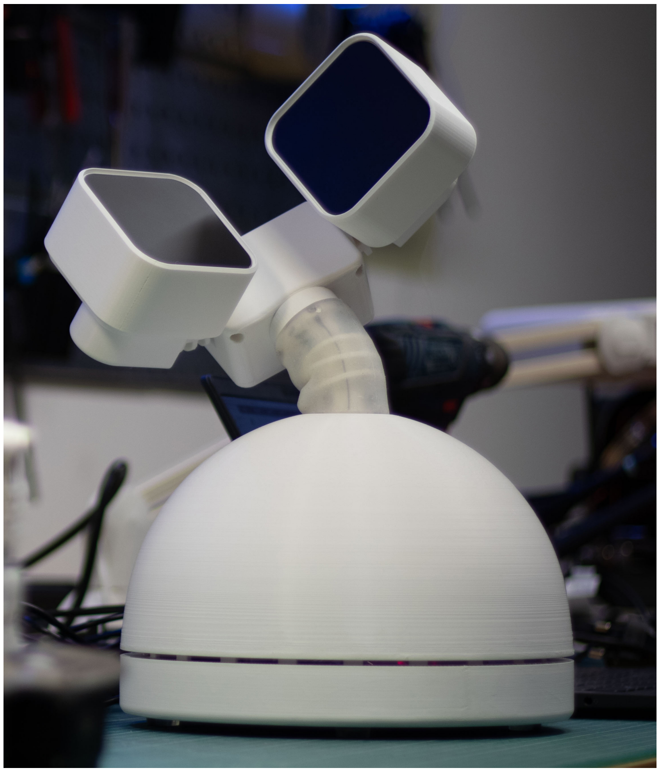

Fig. 1. HARU's revised prototype version incorporating a soft robotic neck for enhanced safety and expressivity.

To investigate embedded sensing within a functional robotic platform, HARU is considered, a tabletop social robot developed for child–robot interaction [11], aligned with UNICEF's policy guidance on artificial intelligence for children [12]. In recent prototypes, HARU's rigid neck and eye joints were replaced by soft continuum actuators to improve safety and expressiveness [13], [14] (Fig. 1). While prior work addressed the design and modeling of these compliant joints, reliable proprioception requires sensors to be integrated directly into the actuator structure without altering its external form. The focus of the present study is the neck joint. Commercial thermoplastic elastomers are used as structural materials, while conductive variants serve as sensing elements. These materials are combined through multi-material 3D printing to embed strain sensors that estimate pitch and roll motions (Fig. 2).

Mapping resistance signals to orientation estimates requires appropriate modeling. Conventional regression approaches do not account for gradual variations such as sensor drift. To address this limitation, machine-learning methods are investigated, with emphasis on continual learning, in which model parameters are updated online while previously

---

[1] Robot Design Lab, Mechatronics Unit, KTH Royal Institute of Technology, SE-10044 Stockholm, Sweden

[2] Honda Research Institute of Japan Co. Ltd., 351-0188, Wako, Japan.
Corresponding Author's Email: `geoand@kth.se`

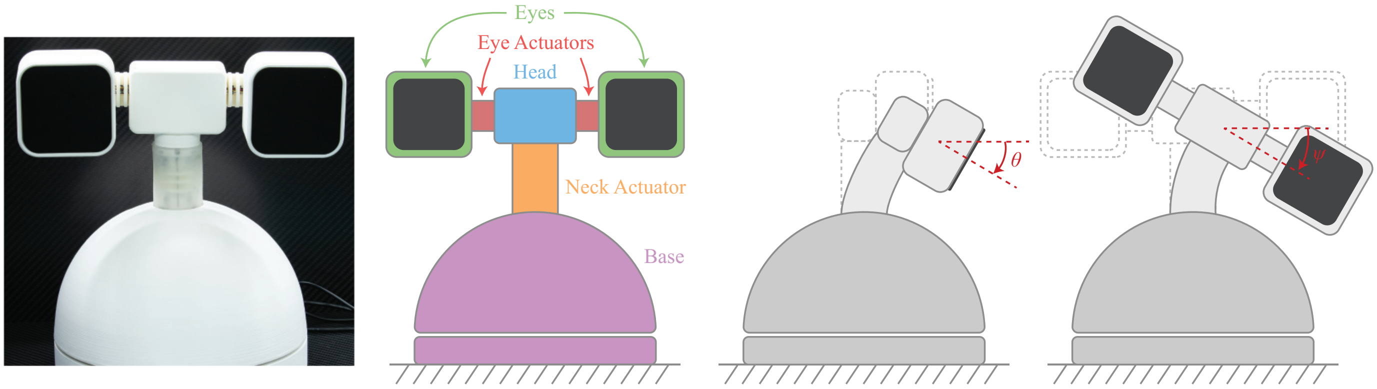

(a) (b) (c) (d)

Fig. 2. (a) HARU's test-rig version developed at the KTH Robot Design Lab for evaluating soft robotic actuators prior to platform integration, (b) conceptual sketch highlighting main components, (c–d) the two dominant neck degrees of freedom considered in this study (pitch θ, roll ψ).

acquired knowledge is retained [15], [16]. Such adaptability is relevant for long-term deployment of soft robotic systems.

Recent studies have combined soft sensing with adaptive or continual learning strategies. An adaptive drift-compensation approach for a soft sensorized finger was presented in [17], demonstrating improved long-term stability. A drift-free latent space representation for soft strain sensors was reported in [18], underscoring the importance of robust signal representations for extended operation. These works motivate the integration of adaptive learning mechanisms within embedded sensing architectures.

In contrast to prior studies where 3D-printed strain sensors were validated primarily as standalone components or in simplified testbeds [5], [6], [8]–[10], the present work integrates sensing directly into a functional soft continuum actuator and evaluates it under realistic robot trajectories. Specifically, (i) a single-step multi-material 3D-printing method is presented for embedding strain sensors without additional assembly; (ii) multiple sensor geometries are statistically evaluated, with a gauge-type pattern selected based on performance metrics; (iii) the optimized sensor array is integrated into HARU's soft neck and validated under structured and randomized motion sequences; and (iv) a continual-learning model is implemented that updates online during operation.

The remainder of this paper is organized as follows: Section II presents the conceptual design of the actuator and sensor geometries. Section III describes the testing and modeling methodology. Section IV details prototype development, Section V reports comparative results, and Section VI concludes with discussion and future directions.

II. CONCEPTUAL DESIGN

A. SCA Base Design

The base soft continuum actuator (SCA) design [13] and its subsequent vibration suppression refinement [19] are illustrated in Fig. 3. The central structural element is a cylindrical continuum core that defines the compliant motion of the actuator. Three spacer discs are distributed along the backbone to maintain structural support and guide four actuation wires. The core is secured to rigid end caps via four mounting holes, enabling bending in two primary planes, pitch (θ) and roll (ψ) (Fig. 2).

The core is coupled to the robot structure through rigid end caps. Actuation is achieved by linear displacement of four wires routed through the spacer discs and driven by motors located beneath the core, resulting in controlled curvature of the compliant backbone. A soft external sleeve encases the structure and is fixed with ring clamps to prevent slippage during operation. The motor assembly is mounted between two plates to maintain alignment and mechanical stability.

B. Sensor Design and Geometric Exploration

To incorporate proprioceptive sensing, the backbone geometry was examined for integration of conductive paths, as shown in Fig. 3. The existing mounting holes were repurposed as electrical terminals, allowing sensor connections without structural modification. Several conductive layouts were evaluated to investigate the influence of geometry on sensing performance, including linear traces of varying widths and a gauge-type pattern.

The objective was to identify geometries capable of stable and repeatable responses under bending while preserving structural compliance. Since mechanical strain distribution affects resistance variation, geometry influences both sensitivity and linearity. Particular attention was given to terminal regions, where electrical contact may introduce instability in printed designs. Additional conductive material was allocated at terminal interfaces to improve contact reliability without altering the external form.

The gauge pattern distributes the conductive path across parallel segments, increasing effective strain during bending and influencing the resulting resistance variation.

C. Sensor Integration

Figure 3 also illustrates integration of the selected gauge pattern into the continuum core. Four sensors are distributed radially along the longitudinal axis, with terminals aligned to the mounting holes. This configuration was selected over a two-sensor alternative to enhance robustness and fault tolerance. Redundancy mitigates variability arising from material

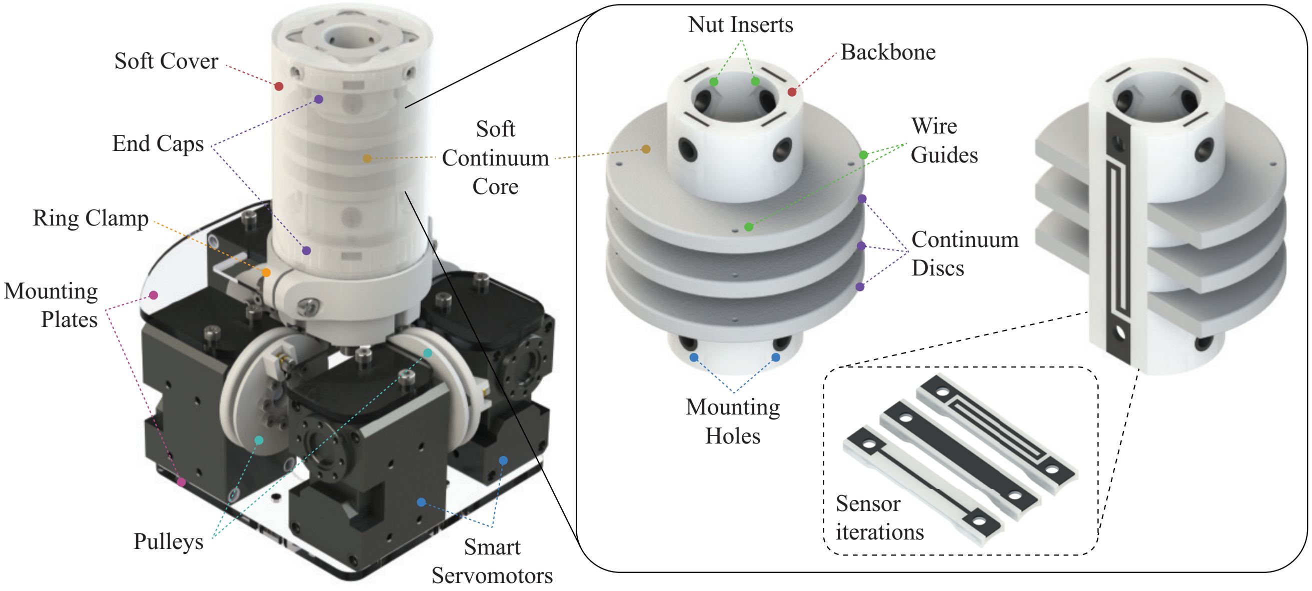

Fig. 3. Integrated overview of the soft continuum actuator (SCA) and embedded sensing concept. (left) Complete SCA module including annotated main components. (center) Detailed view of the soft continuum core and its main geometrical properties. (right) Embedded gauge-type strain sensor integrated along the core, with inset illustrating evaluated sensor geometry iterations (linear and gauge patterns). The SCA design is adapted from [13] and extended with embedded sensing.

inhomogeneities, enables comparison or averaging within each motion plane, and allows continued operation in the event of single-sensor failure.

Under predominantly uniaxial motion (pure pitch or pure roll), the two sensors aligned with the bending plane exhibit opposite resistance variations due to tensile and compressive strain. Sensors aligned orthogonally experience comparatively smaller strain and limited resistance change. This produces anti-symmetric responses in the active pair and near-baseline signals in the orthogonal pair, facilitating differential interpretation and reducing sensitivity to common-mode effects such as temperature variation or material drift.

Following this approach, the integration preserves the external geometry of the actuator while embedding sensing elements within the structure, enabling proprioceptive feedback without altering compliance or appearance.

III. STUDY METHODS

A. Performance Metrics

Data collected from the smart SCA were used for model development and evaluation. After calibration, a continual-learning model was applied in real time, while linear regression and neural network models were constructed for comparison. Prediction quality was assessed using two standard metrics reflecting explanatory power and accuracy.

The coefficient of determination (R^2) quantifies the proportion of variance explained by the model:

$$\mathrm{R}^2 = 1 - \frac{\sum_i (y_i - \hat{y}_i)^2}{\sum_i (y_i - \bar{y})^2}, \qquad (1)$$

where y_i denotes measured values, $\hat{y}_i$ predicted values, and $\bar{y}$ their mean.

The mean absolute error (MAE) measures the average absolute prediction error:

$$\mathrm{MAE} = \frac{\sum_{i=1}^{n} |y_i - \hat{y}_i|}{n}. \qquad (2)$$

B. Sensor Geometry Selection

Three candidate sensor geometries were evaluated prior to integration. Each was subjected to a circular motion profile simultaneously exciting pitch and roll, allowing assessment of linearity and range under combined bending. For each geometry, the R^2 value between measured angles and linear-regression predictions was computed. A one-way analysis of variance (ANOVA) was performed on the resulting R^2 values to test for statistical differences. The geometry with the highest statistical performance was selected for integration into the SCA core.

C. SCA Testing

The selected design was embedded in the actuator core and evaluated under predefined and random motion sequences. Predefined sequences established baseline performance, whereas random trajectories assessed adaptability. Predicted pitch and roll angles were compared with ground-truth measurements obtained from the inertial measurement unit (IMU).

Performance evaluation considered linearity, range, and accuracy. Adaptability of the continual-learning model was examined under random inputs. Stability over time was assessed through repeated experimental sessions, enabling comparison of average R^2 values to identify potential drift or degradation.

D. Model Formulation

All models were trained using data from an initial calibration sequence composed of predefined motion patterns spanning the actuator workspace. This dataset ensured consistent training conditions across modeling approaches. Separate models were trained for pitch (θ) and roll (ψ), mapping the four sensor resistances to a single output angle. This formulation reduces cross-coupling effects and enables direct comparison among modeling strategies.

1) Linear Regression Model: Linear regression was used to model the relationship between sensor resistances and IMU-measured angles. Coefficients were estimated using stochastic gradient descent (SGD) and the Broyden–Fletcher–Goldfarb–Shanno (BFGS) quasi-Newton algorithm. The random seed for SGD minibatch selection was fixed for reproducibility. The general linear model is:

$$\hat{a} = R_1 x_1 + R_2 x_2 + R_3 x_3 + R_4 x_4 + C, \tag{3}$$

where R_i $(i = 1, \ldots, 4)$ denote sensor resistances, x_i regression coefficients, and C a bias term.

2) Neural Network Model: A feed-forward neural network was trained using the same calibration dataset. The network comprised 20 fully connected layers with progressively decreasing width, from 64 neurons in the first hidden layer to 8 neurons before the output layer. Rectified Linear Unit (ReLU) activations were used in hidden layers and a linear activation in the output layer. Bayesian regularization backpropagation was applied to mitigate overfitting given the limited dataset size. This model provides a nonlinear mapping for comparison with linear regression.

3) Continual Learning Model: To accommodate gradual variations in sensor behavior, a continual-learning (CL) approach was implemented. Regression coefficients were updated online as new IMU data became available. Updates were performed using RMSprop, which adapts learning rates based on a moving average of squared gradients:

$$S_{dw} = \beta S_{dw} + (1 - \beta) dw^2, \tag{4}$$

$$w = w - \alpha \cdot \frac{dw}{\sqrt{S_{dw}} + \epsilon}, \tag{5}$$

where S_{dw} denotes the moving average of squared gradients, β the decay factor, α the learning rate, dw the gradient of the loss with respect to weight w, and ϵ a numerical stability constant.

During operation, parameters were updated at the sampling rate of 33 Hz using single-sample updates. At each time step, current sensor readings and corresponding IMU angles were used to compute instantaneous gradients and update parameters. No mini-batching was employed. This fully online scheme reduces memory requirements and enables adaptation to gradual drift.

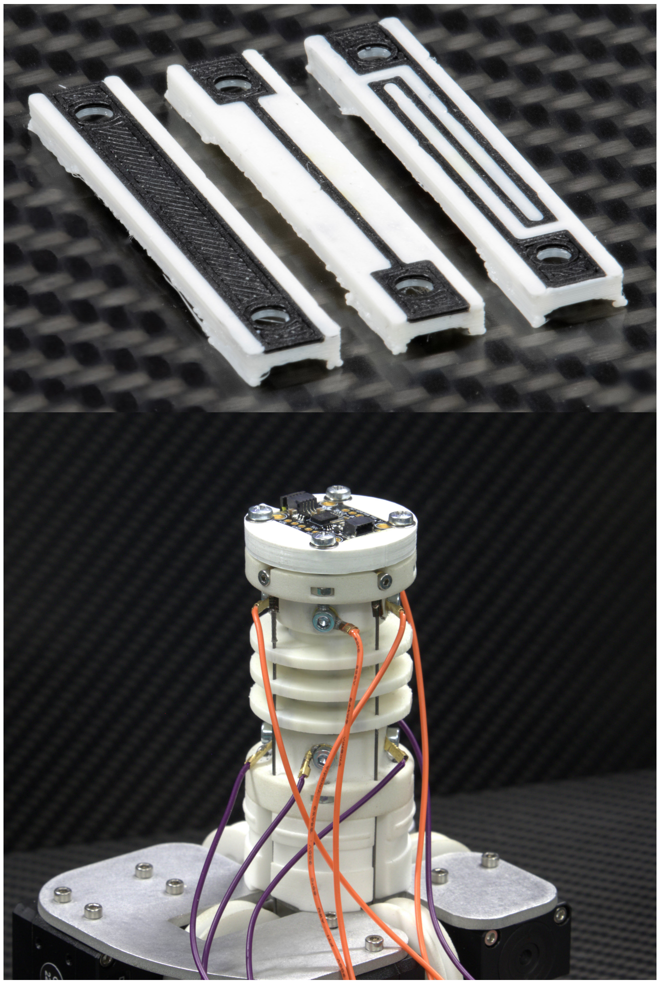

Fig. 4. (top) 3D-printed sensor prototypes fabricated with non-conductive (Shore 85A) and conductive (Shore 90A) TPU, corresponding to the geometries shown in Fig. 3. (bottom) Integrated smart SCA prototype without protective sleeve, with reference IMU mounted at the distal end. Visible wires correspond to temporary signal and ground connections used for evaluation.

E. Experimental Tests and Model Validation

Pre-programmed motion profiles were used to evaluate performance under diverse conditions, including circular, rectangular, diagonal, and single-axis motions. Additional random trajectories were applied to assess adaptability. A single calibrated model per degree of freedom was trained prior to evaluation and tested across all motion profiles. Models were not retrained for individual trajectories, ensuring that reported results reflect generalization rather than trajectory-specific fitting.

IV. PROTOTYPE DEVELOPMENT AND IMPLEMENTATION

To evaluate manufacturability and sensing performance, three sensor prototypes with different conductive geometries were fabricated using flexible thermoplastic polyurethane (TPU) filaments: a non-conductive variant (Shore 85A) and a conductive variant (Shore 90A) (Fig. 4, top). Each prototype included a 0.5 mm thick conductive layer. Two linear patterns (5 mm and 1 mm widths) and one gauge pattern (1 mm traces with 5 mm spacing) were produced. Fabrication was performed on a fused-deposition modeling printer (Raise3D E2) using 90% infill, 0.1 mm layer height, and 107% flow rate to compensate for under-extrusion in flexible filaments. Printing parameters were tuned to match design specifications in mass and dimensions while minimizing artifacts. Electrical continuity was verified after printing, and baseline resistances were recorded. The prototypes were mounted on a test continuum core for initial evaluation.

Following geometry selection, a continuum core integrating four gauge-pattern sensors (as conceptually presented in Fig. 3) was fabricated using the same materials and printing settings. The smart core was mounted on the SCA module (Fig. 4, bottom). Sensor terminals were connected to the data-acquisition system using jumper wires with brass connectors to ensure stable contact with the analogue-to-digital converter (ADC).

The actuator was driven by four Dynamixel XM430-W350-T smart servomotors providing current, position, velocity, and temperature feedback. Daisy-chain communication was used to reduce wiring complexity.

Figure 5 illustrates the electrical configuration. Each embedded strain sensor was connected in a voltage divider with a dedicated reference resistor $R_{ref,i}$ $(i = 1, \dots, 4)$. Reference resistors were selected to match the order of magnitude of nominal sensor resistances R_i to maximize measurement sensitivity. Narrower traces and the gauge pattern exhibited higher nominal resistances due to reduced cross-section and increased conductive path length. Reference resistor values were selected as follows: 3.9 kΩ for the 5 mm linear pattern, 12 kΩ for the 1 mm linear pattern, and 47 kΩ for the gauge configuration. The dividers were supplied with 5 V from a microcontroller unit (MCU), and junction voltages were sampled by the ADC. Sensor upper terminals were connected to ADC inputs and lower terminals to ground.

Ground-truth orientation measurements were obtained using a BNO055 IMU mounted at the distal end of the core (Fig. 4, bottom). Sensor and IMU data were acquired via an Arduino MKR 1010 MCU at 33 Hz and processed on a host computer running MATLAB and Simulink.

Calibration was performed at 33 Hz for approximately 300 s, yielding about 9900 synchronized samples of sensor resistances and IMU-derived angles. Data were not normalized prior to training; instead, learning rates were adjusted to account for resistance magnitudes. No additional filtering beyond the IMU's internal sensor fusion was applied.

All predictive models were implemented within a common software environment. The continual-learning model was updated synchronously at 33 Hz. Hyperparameters were selected empirically, with global learning rate $\alpha = 5 \times 10^{-6}$ and decay factor $\beta = 0.995$. The small learning rate accommodates resistance magnitudes on the order of $10^4\,\Omega$, ensuring stable parameter updates.

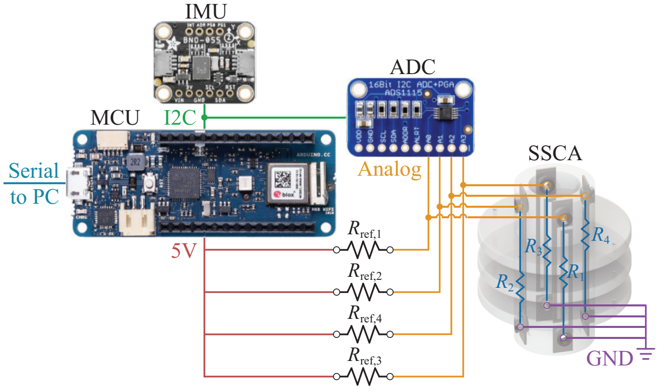

Fig. 5. Electrical wiring diagram of the smart SCA setup showing sensor channels, reference resistors, ADC, IMU, MCU, and servomotor drivers.

TABLE I

AVERAGE R^2 VALUES FOR CANDIDATE SENSOR GEOMETRIES USING LINEAR REGRESSION

Sensor Pattern	θ	ψ
Linear (5 mm)	0.90	0.32
Linear (1 mm)	0.75	0.50
Gauge	0.94	0.79

V. RESULTS

A. Sensor Geometry Selection

Sensor geometry was evaluated using a circular motion profile that excites both degrees of freedom simultaneously, enabling comparison of range and linearity. For each prototype, 500 samples were collected, and R^2 values between measured IMU angles and linear-regression predictions were computed. Results are summarized in Table I.

The gauge configuration yielded the highest R^2 values for both pitch and roll. Its distributed conductive layout increases effective strain under bending and contributes to improved linearity and repeatability. Based on these results, the gauge design was selected for integration and subsequent model comparison.

B. Model Performance Comparison

The integrated SCA with gauge sensors was evaluated under five periodic motion profiles: circular, rectangular, diagonal, pitch-only, and roll-only. Predicted pitch (θ) and roll (ψ) angles from linear regression (LR), neural network (NN), and continual learning (CL) models were compared with IMU measurements. Aggregated results are shown in Fig. 6.

Across trajectories, LR exhibited systematic overshoot and undershoot, particularly near turning points, reflecting limitations of a strictly linear mapping. NN and CL predictions more closely followed IMU measurements. In predominantly uniaxial motions, residual noise was observed in all models, with CL providing the closest agreement. At lower actuation speeds, drift effects were more visible in LR and NN outputs, whereas CL maintained accuracy through online parameter updates.

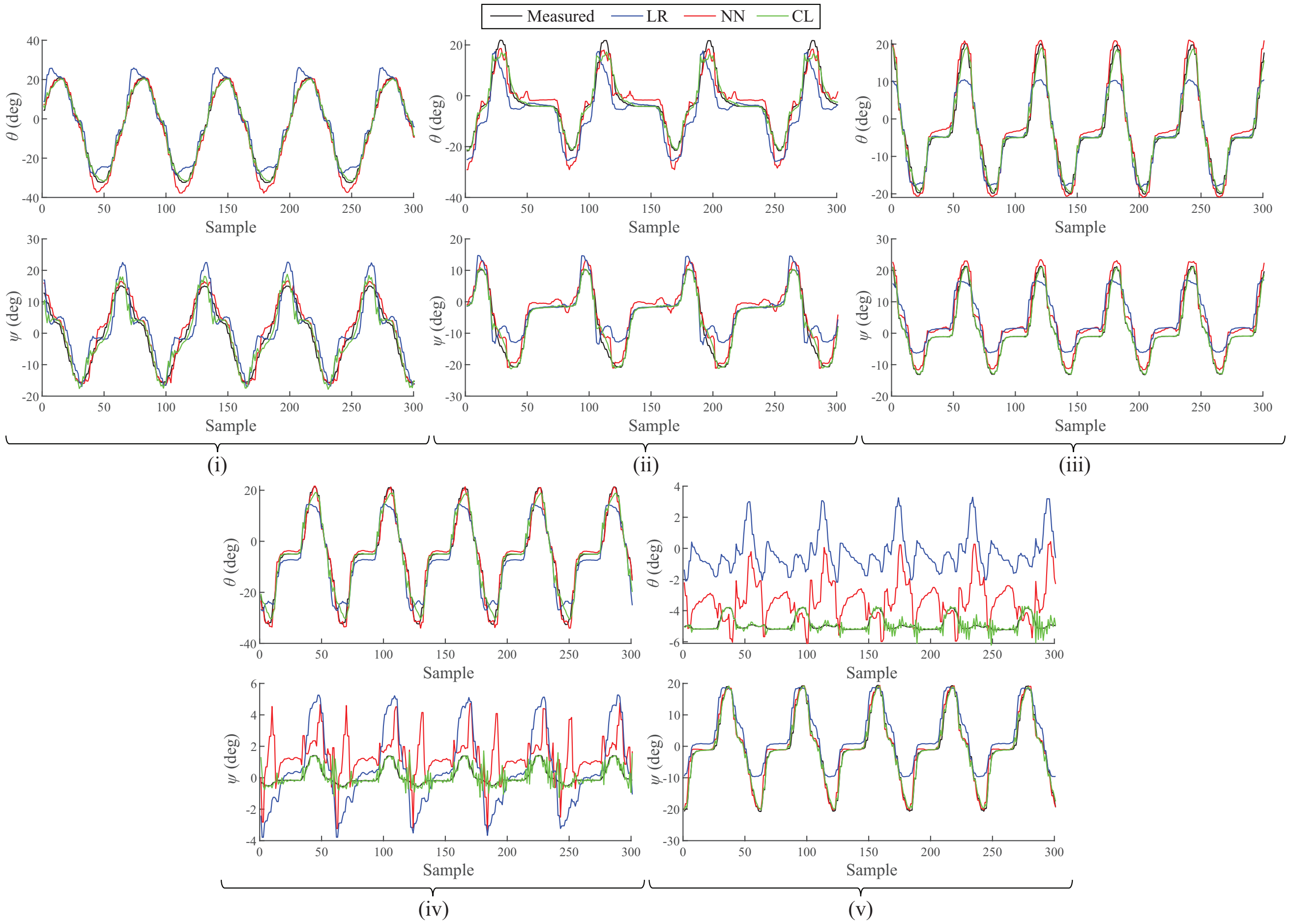

Fig. 6. Aggregated results for pitch (θ) and roll (ψ) across multiple motion profiles. Predictions from linear regression (LR), neural network (NN), and continual learning (CL) models are compared with IMU measurements. Motion sequences include: (i) circular, (ii) rectangular, (iii) diagonal, (iv) pitch-only, and (v) roll-only.

TABLE II

R^2 VALUES BETWEEN PREDICTED AND IMU ANGLES ACROSS THREE EXPERIMENTAL CYCLES.

	Cycle 1	Cycle 2	Cycle 3
Pitch (θ)			
LR	0.89	0.87	0.82
NN	0.97	0.96	0.89
CL	0.99	0.99	0.99
Roll (ψ)			
LR	0.77	0.75	0.81
NN	0.94	0.93	0.95
CL	0.97	0.97	0.98

The R^2 values across three experimental cycles are summarized in Table II, where cycle 1 corresponds to the primary 300-second evaluation dataset. For that cycle, the corresponding Mean Absolute Error (MAE) values were 3.58°, 1.92°, and 0.98° for LR, NN, and CL in pitch, and 3.43°, 1.92°, and 0.86° in roll.

LR consistently produced the lowest R^2 values and the highest MAE values for both degrees of freedom, indicating reduced predictive accuracy. NN improved performance relative to LR, reflecting the benefit of nonlinear mapping. CL achieved the highest R^2 values across all cycles, with values above 0.97 for roll and near 0.99 for pitch.

Across experimental cycles, LR exhibited the largest variability, particularly in roll. NN maintained relatively high performance with moderate variation between sessions, while CL remained consistently accurate, with only minor variation across cycles. These results indicate stable performance of the continual-learning approach under gradual changes in sensor behavior.

C. Performance Under Randomized Motion

The SCA was further evaluated under manually generated high-frequency random motions to assess robustness under non-periodic excitation. A 100-sample excerpt of pitch and roll predictions is shown in Fig. 7. Under randomized inputs, LR and NN exhibited larger overshoot and undershoot relative to IMU measurements. NN performance degraded due to its fixed parameters, whereas CL maintained stable predictions through online adaptation. These results indicate improved robustness of the continual-learning model under irregular motion conditions.

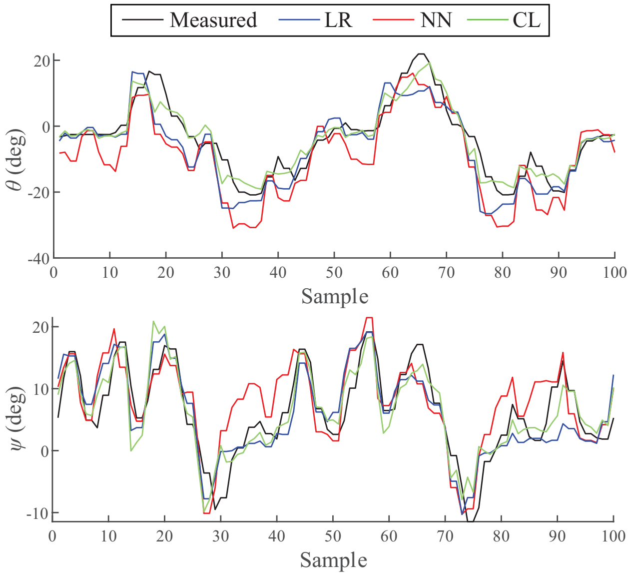

Fig. 7. Model comparison under randomized motion sequences for pitch (θ) and roll (ψ).

VI. CONCLUSIONS

The development and evaluation of a multi-material 3D-printed soft sensor integrated into a soft continuum actuator serving as the robotic neck of the HARU platform were presented. Flexible and conductive filaments were combined to embed strain sensors within the actuator without altering its external geometry. Multiple sensor layouts were examined, and a gauge-type pattern arranged in a cross-configuration was selected for measuring two degrees of freedom.

The integrated sensor array enabled proprioceptive feedback within a functional soft actuator, extending prior work in which 3D-printed sensors were primarily evaluated in isolation. Sensor data were modeled using linear regression, a static neural network, and a continual-learning framework. Across trajectories, randomized motions, and repeated experimental sessions, the continual-learning model achieved the highest predictive accuracy, with $R^2 > 0.97$ and mean absolute errors below $1°$. These results indicate that online adaptation effectively compensates for sensor nonlinearities, inter-trial variability, and gradual material changes, supporting reliable proprioception in soft robotic systems.

Optimization-based online adaptation methods may, however, be affected by gradual forgetting if the data distribution changes significantly. In this study, drift occurred slowly, allowing RMSprop-based updates to track parameter variations. Abrupt or strongly non-stationary conditions could degrade previously learned mappings. Incorporating regularization, replay, or consolidation mechanisms may improve long-term knowledge retention in future implementations.

ACKNOWLEDGEMENTS

The authors acknowledge that ChatGPT (OpenAI, GPT-5, accessed September 2025) was utilized only for refining the grammar and clarity of the text originally drafted by the authors. No AI-generated content was used to create new text, generate ideas, or contribute in any way to the research findings or interpretations.

REFERENCES

[1] D. Rus and M. T. Tolley, “Design, fabrication and control of soft robots,” *Nature*, vol. 521, no. 7553, pp. 467–475, 2015.

[2] Y. Zhu, W. Gong, K. Chu, X. Wang, Z. Hu, and H. Su, “A novel wearable soft glove for hand rehabilitation and assistive grasping,” *Sensors*, vol. 22, no. 16, p. 6294, 2022.

[3] K. C. Galloway, K. P. Becker, B. Phillips, J. Kirby, S. Licht, D. Tchernov, R. J. Wood, and D. F. Gruber, “Soft robotic grippers for biological sampling on deep reefs,” *Soft robotics*, vol. 3, no. 1, pp. 23–33, 2016.

[4] C. B. Teeple, R. C. S. Louis, M. A. Graule, and R. J. Wood, “The role of digit arrangement in soft robotic in-hand manipulation,” in *2021 IEEE/RSJ International Conference on Intelligent Robots and Systems (IROS)*. IEEE, 2021, pp. 7201–7208.

[5] S. Mousavi, D. Howard, F. Zhang, J. Leng, and C. H. Wang, “Direct 3d printing of highly anisotropic, flexible, constriction-resistive sensors for multidirectional proprioception in soft robots,” *ACS Applied Materials & Interfaces*, vol. 12, no. 13, pp. 15 631–15 643, 2020.

[6] A. Georgopoulou, L. Egloff, B. Vanderborght, and F. Clemens, “A sensorized soft pneumatic actuator fabricated with extrusion-based additive manufacturing,” *Actuators*, vol. 10, no. 5, p. 102, 2021.

[7] S. T. Muralidharan, G. Andrikopoulos, and L. Feng, “A survey on the current trends and applications of design optimization for compliant and soft robotics,” in *2023 IEEE/ASME International Conference on Advanced Intelligent Mechatronics (AIM)*, 2023, pp. 47–53.

[8] M. Borghetti, M. Serpelloni, E. Sardini, and S. Pandini, “Mechanical behavior of strain sensors based on pedot: Pss and silver nanoparticles inks deposited on polymer substrate by inkjet printing,” *Sensors and Actuators A: Physical*, vol. 243, pp. 71–80, 2016.

[9] J. Gooding and T. Fields, “3d printed strain gauge geometry and orientation for embedded sensing,” in *58th AIAA/ASCE/AHS/ASC Structures, Structural Dynamics, and Materials Conference*, 2017, p. 0350.

[10] H. Liu, H. Zhang, W. Han, H. Lin, R. Li, J. Zhu, and W. Huang, “3d printed flexible strain sensors: from printing to devices and signals,” *Advanced Materials*, vol. 33, no. 8, p. 2004782, 2021.

[11] R. Gomez, D. Szapiro, K. Galindo, and K. Nakamura, “Haru: Hardware design of an experimental tabletop robot assistant,” in *Proceedings of the 2018 ACM/IEEE International Conference on Human-Robot Interaction*, ser. HRI ’18. New York, NY, USA: Association for Computing Machinery, 2018, p. 233–240. [Online]. Available: https://doi.org/10.1145/3171221.3171288

[12] K. P. Virginia Dignum, Melanie Penagos and S. Vosloo. (2021. [Online], Nov) "policy guidance on ai for children". [Online]. Available: https://www.unicef.org/globalinsight/reports/policy-guidance-ai-children

[13] G. Andrikopoulos, L. Hassler, and R. Gomez, “On the design of a soft robotic neck for the social robot haru,” *presented in ICRA 2023 Workshop: Towards a Balanced Cyberphysical Society - A Focus on Group Social Dynamics, London, UK*, 29 May - 2 June 2023.

[14] A. Lindestam, S. T. Muralidharan, G. Andrikopoulos, and R. Gomez, “Model identification of a soft robotic eye actuator for safe social interactions,” in *2024 IEEE International Conference on Advanced Intelligent Mechatronics (AIM)*, 2024, pp. 211–216.

[15] F. Piqué, H. T. Kalidindi, L. Fruzzetti, C. Laschi, A. Menciassi, and E. Falotico, “Controlling soft robotic arms using continual learning,” *IEEE Robotics and Automation Letters*, vol. 7, no. 2, pp. 5469–5476, 2022.

[16] H. Bae, S. Song, and J. Park, “The present and future of continual learning,” in *2020 International Conference on Information and Communication Technology Convergence (ICTC)*, 2020, pp. 1193–1195.

[17] N. Kushawaha, R. Pathan, N. Pagliarani, M. Cianchetti, and E. Falotico, “Adaptive drift compensation for soft sensorized finger using continual learning,” in *2025 IEEE 8th International Conference on Soft Robotics (RoboSoft)*. IEEE, 2025, pp. 1–6.

[18] T. G. Thuruthel, K. Gilday, and F. Iida, “Drift-free latent space representation for soft strain sensors,” in *2020 3rd IEEE International Conference on Soft Robotics (RoboSoft)*. IEEE, 2020, pp. 138–143.

[19] S. T. Muralidharan, R. Gomez, and G. Andrikopoulos, “On vibration suppression of a tendon-driven soft robotic neck for the social robot haru,” *Frontiers in Robotics and AI*, vol. 12, p. 1698343, 2025.